

Article ID: 1000-7032(2024)09-1511-10

## High Sensitivity Submicron Scale Temperature Sensor Based on Perovskite Nanoplatelet Lasers

ZHAO Ruofan<sup>1</sup>, TAO Jianxun<sup>1</sup>, XI Yuying<sup>1</sup>, CHEN Jiangzhao<sup>2</sup>, JI Ting<sup>1</sup>,  
WANG Wenyan<sup>1</sup>, WEN Rong<sup>1</sup>, CUI Yanxia<sup>1,3</sup>, CHEN Junsheng<sup>4\*</sup>, LI Guohui<sup>1,3\*</sup>

(1. College of Electronic Information and Optoelectronic Engineering, Taiyuan University of Technology, Taiyuan 030024, China;

2. School of Materials Science and Engineering, Kunming University of Science and Technology, Kunming 650093, China;

3. Shanxi-Zheda Institute of Advanced Materials and Chemical Engineering, Taiyuan 030024, China;

4. Nano-Science Center & Department of Chemistry, University of Copenhagen, Copenhagen DK-2100, Denmark)

\* Corresponding Authors, E-mail: JunSheng.Chen@chem.ku.dk; liguohui@tyut.edu.cn

**Abstract:** Submicron scale temperature sensors are crucial for a range of applications, particularly in micro and nanoscale environments. One promising solution involves the use of active whispering gallery mode (WGM) microresonators. These resonators can be remotely excited and read out using free-space structures, simplifying the process of sensing. In this study, we present a submicron-scale temperature sensor with a remarkable sensitivity up to 185 pm/°C based on a triangular MAPbI<sub>3</sub> nanoplatelet (NPL) laser. Notably, as temperature changes, the peak wavelength of the laser line shifts linearly. This unique characteristic allows for precise temperature sensing by tracking the peak wavelength of the NPL laser. The optical modes are confined within the perovskite NPL, which measures just 85 nm in height, due to total internal reflection. Our NPL laser boasts several key features, including a high *Q* of ~2 610 and a low laser threshold of about 19.8 μJ·cm<sup>-2</sup>. The combination of exceptional sensitivity and ultra-small size makes our WGM device an ideal candidate for integration into systems that demand compact temperature sensors. This advancement paves the way for significant progress in the development of ultrasmall temperature sensors, opening new possibilities across various fields.

**Key words:** temperature sensor; submicron scale; perovskite nanoplatelet

**CLC number:** TP212.11; O482.31

**Document code:** A

**DOI:** 10.37188/CJL.20240133

## 基于钙钛矿纳米片激光器的高灵敏度亚微米级温度传感器

赵若凡<sup>1</sup>, 陶健勋<sup>1</sup>, 邵育莺<sup>1</sup>, 陈江照<sup>2</sup>, 冀婷<sup>1</sup>, 王文艳<sup>1</sup>, 温荣<sup>1</sup>,  
崔艳霞<sup>1,3</sup>, 陈俊生<sup>4\*</sup>, 李国辉<sup>1,3\*</sup>

(1. 太原理工大学电子信息与光学工程学院, 山西 太原 030024; 2. 昆明理工大学材料科学与工程学院, 云南 昆明 650093;

3. 山西浙大新材料与化工研究院, 山西 太原 030024; 4. 丹麦哥本哈根大学 纳米科学中心及化学系, 丹麦 哥本哈根 DK-2100)

**摘要:** 在微纳米尺度环境中, 亚微米级温度传感器的应用扮演着至关重要的角色。特别地, 采用主动型回音

收稿日期: 2024-05-13; 修訂日期: 2024-05-26

基金项目: 国家自然科学基金(U21A20496, 61905173, 12104334); 山西省重点研发计划(202102150101007); 山西省留学回国人员科技活动择优资助项目(20230011); 山西浙大新材料与化工研究院研发项目(2021SX-FR008, 2022SX-TD020); 中央引导地方科技发展资金项目(YDZJSX20231A010, YDZJSX2021A012); 山西省自然科学基金(20210302123154, 202203021222102); 山西省回国留学人员科研资助项目(2021-033); 量子光学与量子光学器件国家重点实验室项目(KF202306); 诺和诺德基金会(NNF22OC0073582)

Supported by National Natural Science Foundation of China (U21A20496, 61905173, 12104334); The key Research and Development Program of Shanxi Province (202102150101007); Fund Program for the Scientific Activities of Selected Returned Overseas Professionals in Shanxi Province (20230011); Research Program Supported by Shanxi-Zheda Institute of Advanced Materials and Chemical Engineering (2021SX-FR008, 2022SX-TD020); the Central Government Guides Local Funds for Scientific and Technological Development (YDZJSX20231A010, YDZJSX2021A012); the Natural Science Foundation of Shanxi Province (20210302123154, 202203021222102); Research Project Supported by Shanxi Scholarship Council of China (2021-033); State key laboratory program of quantum optics and quantum optics devices (KF202306); the Novo Nordisk Foundation (NNF22OC0073582)

壁模式(WGM)的微纳谐振腔设计能够通过自由空间结构实现传感信号的远程激发与探测,极大地促进了传感过程的便捷性和可行性。本文展示了一种基于 $\text{MAPbI}_3$ 三角形纳米片(NPL)激光器的亚微米级温度传感器,其灵敏度高达 $185 \text{ pm}/\text{C}$ 。实验研究表明,激光发射的中心波长与环境温度之间存在紧密且稳定的线性关系,这一发现为通过监测谐振波长变化来实现高精度温度测量提供了有力支持。光学模式得益于全内反射效应,被有效地局限在仅 $85 \text{ nm}$ 厚的纳米片内部。该NPL激光器展现出杰出的性能特性,其品质因数( $Q$ )高达约2 610,阈值低至 $19.8 \mu\text{J}\cdot\text{cm}^{-2}$ 。高灵敏度和小尺寸使钙钛矿纳米片成为集成温度传感器的理想器件。这一研究有望加速超小型温度传感器的技术进步,拓展其在光电技术领域的应用范畴,开创更多创新可能。

关 键 词: 温度传感器; 亚微米; 钙钛矿纳米片

## 1 Introduction

Temperature, as a basic physical parameter, is important in many applications<sup>[1-3]</sup>. Conventional temperature sensors are not able to measure temperature fluctuations in small regions, especially on the submicron scale<sup>[4-5]</sup>. The demand for reliable, fast, and precise thermal sensors with ultrasmall size has garnered significant attention in the fields of chemical, mechanical, and material engineering<sup>[6]</sup>. Over the decades, temperature sensors based on tapered fiber optics<sup>[7-8]</sup> or waveguide coupling configurations<sup>[9-10]</sup> have been developed for thermal sensing. However, most of these sensors are bulky and difficult to apply in micro and nanoscale sample environments<sup>[11-13]</sup>.

Optical microresonators are expected to overcome these limitations<sup>[14]</sup>. Among various optical microresonators, whispering gallery mode (WGM) microresonators have gained increasing attention and undergone significant development due to their high-quality factors ( $Q$ ) and small size. Among them, light circulates in these resonators through total internal reflection, which significantly enhances the interaction between light and matter and promotes integration<sup>[15-16]</sup>. Resonant wavelength ( $\lambda$ ) of WGM microcavity determined by refractive index ( $n$ ) and cavity length ( $L$ ), usually expressed as  $\lambda = 2nL/p$ , where  $p$  is an integer. Due to the sensitivity of  $n$  and  $L$  to temperature ( $T$ ), the peak wavelength shift caused by temperature variation can be defined as<sup>[17]</sup>:

$$d\lambda = \lambda \left( \frac{1}{n} \frac{dn}{dT} + \frac{1}{L} \frac{dL}{dT} \right) dT, \text{ where } dn/dT \text{ is the thermal-optical (TO) coefficient, and } dL/dT \text{ is the thermal-expansion (TE) coefficient}^{[18]}.$$

For most inorgan-

ic semiconductors and also for methylamine halide perovskite, the contribution of the TE coefficient is smaller than that of the TO coefficient<sup>[14]</sup>. Therefore, cavity materials with larger TO coefficients are favorable for developing temperature sensors with high sensitivity. Various WGM microresonators have been successfully demonstrated for temperature sensing, typically made of silica<sup>[19]</sup>. Because of the low TO coefficient ( $\sim 1 \times 10^{-5} \text{ K}^{-1}$ ) of silica, the temperature sensitivities of sensors based on silica resonators are limited to about  $\sim 64 \text{ pm}/\text{C}$ <sup>[20]</sup>. To improve the sensitivity, silica was usually enclosed by materials with large negative TO coefficient, including PD-MS<sup>[19]</sup>, lithium niobate<sup>[21]</sup>, and dye-doped polymer<sup>[13]</sup>, which significantly increases the complexity of these sensors' fabrication. In addition to this, almost all WGM temperature sensors based on passive microresonator use fiber tapers<sup>[20]</sup>, waveguide or prism<sup>[22]</sup> for resonance detection and readout, which makes the whole device bulky and highly susceptible to mechanical perturbations<sup>[14]</sup>.

Temperature sensors based on active microresonator that are compatible with free-space excitation and readout optics, greatly simplify system implementation<sup>[17]</sup>. Furthermore, active WGM microresonators, which can confine light in a submicron-scale region through total internal reflection, facilitate the integration with micro and nanoscale environments<sup>[23]</sup>. Traditionally, active WGM microresonators have been realized by combining high- $Q$  microresonators with a gain medium layer<sup>[24]</sup>, e. g., combining the WGM microresonators with fluorophores, rare earth elements, dyes or other types of gain medium<sup>[25-27]</sup>. The active WGM microresonators that have

been demonstrated are not only robust and compact but also possess high  $Q$ , making them highly suitable for temperature sensing applications. However, several problems still exist. Firstly, the sizes of active WGM microcavities temperature sensors demonstrated in measuring submicron-scale temperature fluctuations in previous reports<sup>[24-27]</sup> are still on the micron scale, which makes integration and scalability in submicron-scale environments applications challenging<sup>[14]</sup>. Secondly, the thresholds of those active WGM resonators are still high ( $> 840 \mu\text{J cm}^{-2}$ )<sup>[28]</sup>, which may damage the samples in biomonitoring. Lastly, the temperature sensitivities of those active WGM resonators are still low ( $\sim 40 \text{ pm}/^\circ\text{C}$ )<sup>[29]</sup>. Therefore, it is urgent to develop active temperature sensors on the submicron scale with a low threshold and high sensitivity.

Metal halide perovskites are considered as promising low-cost semiconductor materials<sup>[30]</sup>. Among various perovskite materials, organic-inorganic hybrid materials, with MAPbI<sub>3</sub> as a representa-

tive, are of particular interest in the fields of semiconductor lasers as well as solar cells<sup>[31]</sup>, light emitting diodes<sup>[32]</sup>, photodetectors<sup>[33]</sup>, etc., due to their large absorption coefficients, exceptionally low trap-state densities, large charge carrier diffusion lengths, and high charge mobilities. The low temperature solution processability of perovskites has attracted widespread interest in developing low-cost optoelectronic devices<sup>[34-36]</sup>. In particular, methylammonium lead halide ( $\text{CH}_3\text{NH}_3\text{PbX}_3$ ,  $X = \text{Cl}, \text{Br}, \text{I}$ ) has proven to be a promising material for lasers<sup>[37]</sup>. Most importantly, they have large negative TO coefficients ( $\sim -3 \times 10^{-4} \text{ K}^{-1}$ )<sup>[38]</sup>, which makes them a promising material for developing temperature sensors. However, temperature sensors based on perovskite lasers have not been reported yet. Tab. 1 shows the comparison of MAPbI<sub>3</sub> NPL based devices. This work lays a solid foundation for the development and application of thermal sensing based on NPL and other metal-halide materials.

Tab. 1 Comparison of MAPbI<sub>3</sub> NPL based devices

Type of laser	Substrate	Edge length/ $\mu\text{m}$	Thickness/nm	$P_{\text{th}}/(\mu\text{J}\cdot\text{cm}^{-2})$	$Q$
Photonic laser <sup>[39]</sup>	Mica	28	150	40	650
Photonic laser <sup>[18]</sup>	100 nm SiO <sub>2</sub> -diamond	29	80	52. 19	1 962
Plasmonic laser <sup>[40]</sup>	10 nm SiO <sub>2</sub> -Au	10	50	59. 2	—
Photonic laser	Mica	36	85	19. 8	2 610

This work demonstrated a temperature sensor with sensitivity as high as  $185 \text{ pm}/^\circ\text{C}$  based on a MAPbI<sub>3</sub> nanoplatelet (NPL), which has a side length of  $36 \mu\text{m}$  and a thickness of  $85 \text{ nm}$ . The NPL also features a low lasing threshold down to  $\sim 19.8 \mu\text{J}\cdot\text{cm}^{-2}$ , which is tens of times lower than that of the counterparts reported in previous reports<sup>[28]</sup>. The center wavelength of the laser line remains constant for more than  $150 \text{ s}$  of continuous operation, indicating that it has good stability, thus ensuring the robustness of the temperature sensor. The central peak of the laser can be restored when the temperature returns to its initial value. The developed nanolaser temperature sensor with high sensitivity, ease of fabrication and ultrasmall size can have many potential applications in thermometry, such as WGM barcode techniques<sup>[41]</sup>, monitoring of superconductors<sup>[42]</sup>, bio-

physical sensors<sup>[43]</sup>, etc.

## 2 Experiment

Schematic diagram of the temperature sensor based on a perovskite NPL laser is shown in Fig. 1. The MAPbI<sub>3</sub> nanoplatelets used in our study were synthesized by the two-step chemical vapor deposition method (CVD), which includes a first step of growing PbI<sub>2</sub> nanoplatelets and a second step of converting PbI<sub>2</sub> nanoplatelets into MAPbI<sub>3</sub> nanoplatelets<sup>[44]</sup>.

The emission spectra at different temperatures were measured with a homemade microscopic photoluminescence measurement system. The perovskite NPL was excited by a femtosecond laser beam (wavelength of  $343 \text{ nm}$ , pulse width of  $\sim 290 \text{ fs}$ ), which was focused down to a beam radius of  $57 \mu\text{m}$

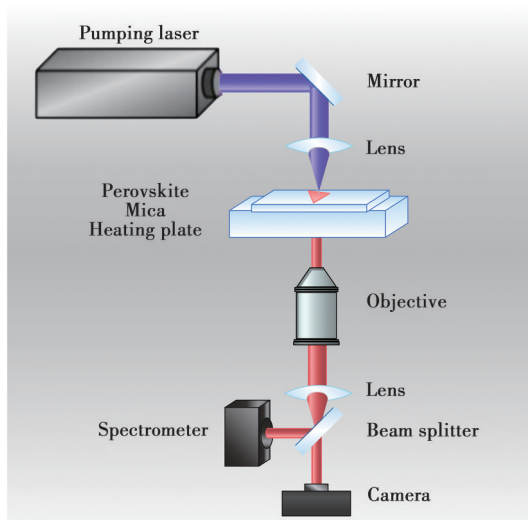


Fig. 1 Schematic diagram of experimental setup for the perovskite NPL laser-based temperature sensor

by a convex lens ( $f = 20$  cm). The position of the NPL was precisely controlled by high-resolution three-axis micro-positioning stages. The emission from NPL was collected by a microscopic objective lens and split into two beams by a beam splitter. One was sent into a spectrometer (wavelength resolution  $\sim 0.07$  nm). The other one was sent to a sCMOS camera. The NPL is housed in a sealed box and is configured with a silicon diode thermometer and a  $50\text{-}\Omega$  heater to achieve precise control of the sample's temperature. Based on the voltage-temperature characteristic curve of the silicon diode, the

temperature at the sample location can be monitored and controlled in real time with an uncertainty of  $0.1^\circ\text{C}$ .

### 3 Results and Discussion

The microscopic image of a perovskite NPL is shown in Fig. 2 (a). As can be seen, the NPL has regular and unwrinkled facets with a side length of  $36\text{ }\mu\text{m}$ . The cross-sectional view recorded by the atomic force microscope showed that NPL could be as thin as  $85\text{ nm}$ . Gaussian fit is used to obtain the full width at half maxima (FWHM) linewidth below the laser threshold and Lorentzian fit is used to obtain the FWHM linewidth above the threshold. These methods are widely used in laser emission spectra analyses<sup>[18,44]</sup>. Fig. 2 (b) shows the emission spectra of the NPL at different pump intensities. At low pump density ( $P \sim 19.8\text{ }\mu\text{J}\cdot\text{cm}^{-2}$ ), it shows a broad Gaussian line profile with a FWHM linewidth of  $\sim 30\text{ nm}$ . When the  $P$  exceeded  $19.8\text{ }\mu\text{J}\cdot\text{cm}^{-2}$ , three narrow peaks with Lorentz line shape centered at  $783\text{ nm}$  (fundamental WGM mode),  $781.13\text{ nm}$  (first-order WGM mode), and  $785.3\text{ nm}$  (first-order WGM mode) with a FWHM linewidth of  $\sim 0.3\text{ nm}$  appeared on top of the spontaneous emission, which is the strong evidence of lasing. The change in the effective refractive index causes the variations in

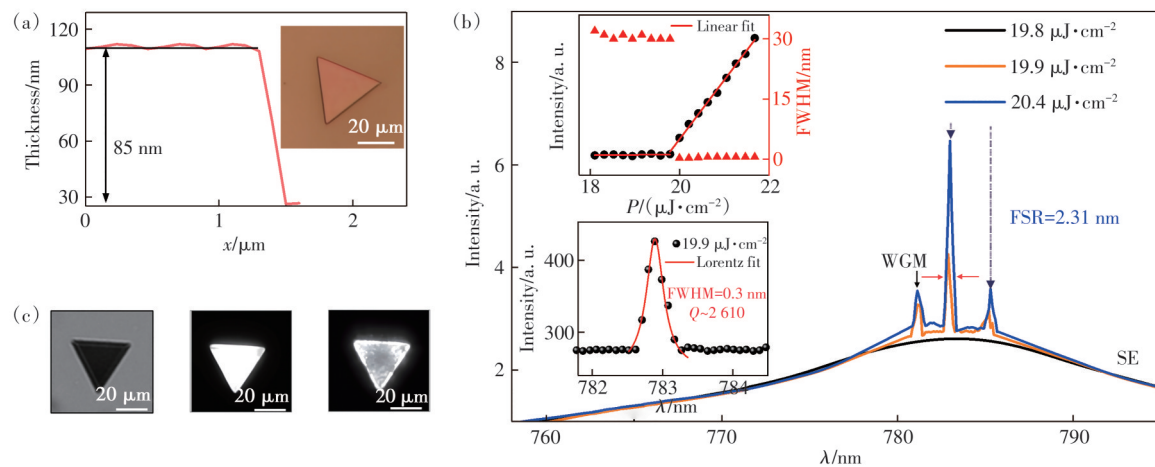


Fig. 2 (a) AFM cross section of the perovskite NPL shows that the thickness is  $85\text{ nm}$ . Inset: image of NPL with an edge length of  $36\text{ }\mu\text{m}$ . (b) The photoluminescence spectra of NPL near the lasing threshold. Inset: dependence of output intensity and FWHM of the NPL on the pump density ( $P$ ), Lorentzian fit FWHM width of  $\sim 0.3\text{ nm}$ . (c) Optical image of the NPL under illumination with white light (left) and laser light at pump densities of  $P = 19\text{ }\mu\text{J}\cdot\text{cm}^{-2}$  (below threshold) and  $P = 20.4\text{ }\mu\text{J}\cdot\text{cm}^{-2}$  (above threshold)

wavelength between the fundamental mode and higher-order modes<sup>[44]</sup>.

The corresponding  $Q$  ( $Q = \lambda/\Delta\lambda$ )<sup>[45]</sup> is  $\sim 2610$ . The spacing between two adjacent peaks, which is called free space range (FSR), is almost the same ( $\sim 2.31$  nm) because the higher-order modes on both sides of the fundamental mode are of the same order. The FSR can also be calculated by equation  $\Delta\lambda = \lambda^2/na$ ,  $a$  and  $n$  denote the side length and effective refractive index of the triangular-shaped NPL, respectively<sup>[44]</sup>. According to the edge length (36  $\mu\text{m}$ ) of NPL, the theoretical FSR should be 2.31 nm which is very consistent with the measured value (2.31 nm, Fig. 2(b)). The inset in Fig. 2(b) shows the functional relationship between the light-in and light-out data. A linear fit to the output intensity reveals a kink at the threshold ( $19.8 \mu\text{J}\cdot\text{cm}^{-2}$ ). The spectral changes further confirm the laser threshold ( $P_{\text{th}}$ ) of NPL is  $19.8 \mu\text{J}\cdot\text{cm}^{-2}$ . Together with the intensity change, the FWHM suddenly changes from

$\sim 31$  nm to  $0.3$  nm. The two regimes correspond to spontaneous emission (below  $P_{\text{th}}$ ) and stimulated emission (above  $P_{\text{th}}$ ), respectively. Furthermore, we observe different photoluminescence intensity distributions between excitation light intensity below and above  $P_{\text{th}}$ : below  $P_{\text{th}}$  NPL shows uniform photoluminescence intensity (middle images in Fig. 2(c)); above  $P_{\text{th}}$  NPL shows strong photoluminescence with spatial interference from the edge of NPL (right image in Fig. 2(c)), which is because of the light fields reflected between the NPL surfaces forms a well-confined inside the cavity.

Fig. 3 (a) shows the evolution of the lasing spectra of NPLs as temperatures ( $T$ ) rise from 21 °C to 25 °C. All modes exhibit a blueshift with increasing  $T$ . Specifically, the laser wavelength is 785.03 nm at 21 °C. When the temperature rises to 25 °C, the laser wavelength shifts to 784.29 nm. Fig. 3(b) shows the peak wavelength shift with temperature. It can be seen that the peak wavelength varies

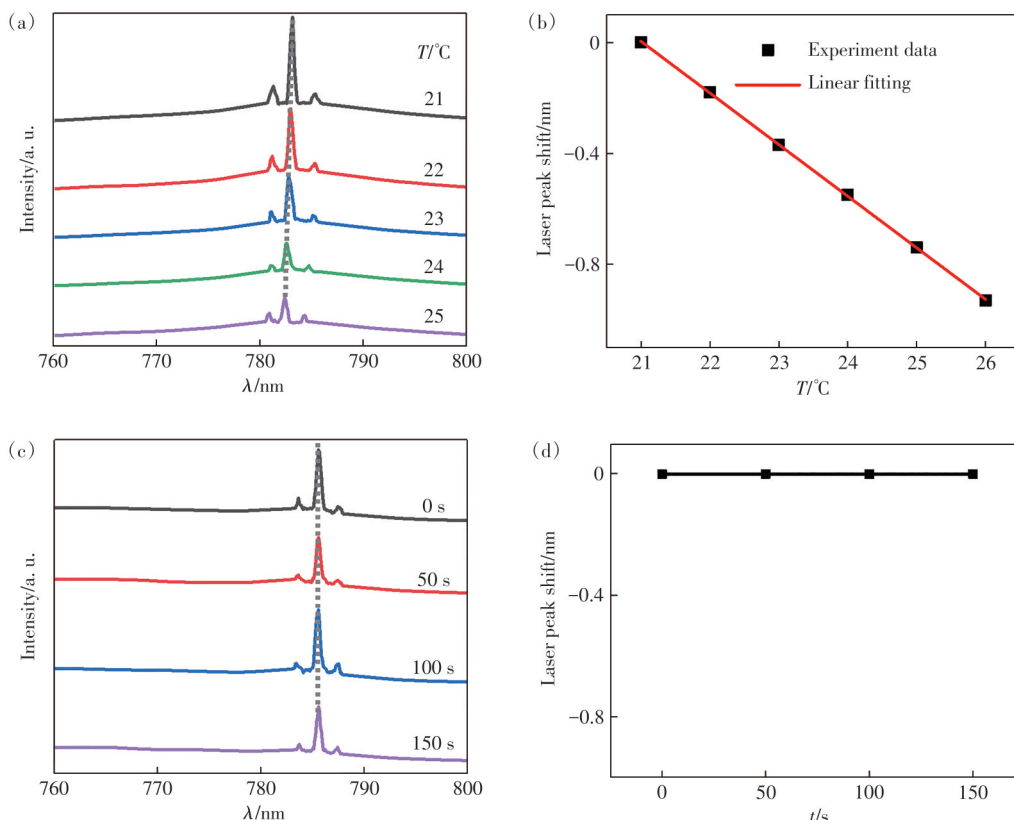


Fig. 3 (a) The evolution of the lasing spectra of perovskite triangular NPLs with temperature. (b) The dependence of the laser peaks on temperature shows that the peak wavelength shifts linearly with temperature with a coefficient of  $\sim 185 \text{ pm}/^\circ\text{C}$ . (c) The dependence of the spectra of the NPL laser on time. (d) The dependence of the peak wavelength of the NPL laser on time

linearly with increasing temperature. Tab. 2 shows the NPL temperature varies with heating plate. For convenience, all the set temperatures are integers. By fitting and analyzing the experimental data, the sensitivity is obtained to be  $(0.185 \pm 0.005)$  nm/ $^{\circ}\text{C}$ . The maximum deviation of temperature measured the NPL from the setting temperature is around  $0.03\ ^{\circ}\text{C}$ .

Tab. 2 Comparison of the set heating temperature and the NPL temperature

Set heating temperature/ $^{\circ}\text{C}$	Temperature of the NPL/ $^{\circ}\text{C}$	Laser peak shift/nm
21	21	0
22	21.97	-0.18
23	23	-0.37
24	23.97	-0.55
25	25	-0.74
26	26.03	-0.93

Compared with the previous temperature sensors based on active WGM resonators<sup>[24, 26, 29]</sup>, the temperature sensor based on perovskite nanoplatelet lasers has high temperature sensitivity, while avoiding sophisticated fabrication processes and high pumping power. The high sensitivity of the fabricated temperature sensor based on perovskite NPL can be attributed to the tight confinement of the optical modes within NPL and effective thermal conductivity *via* a large contacting surface between NPL and heating plate. The laser peaks are blueshifted as the temperature increases, unlike some conventional semiconductors, such as Si, Ge, and GaAs, which are redshifted as the temperature increases<sup>[30]</sup>. The blue-shift in perovskite NPL laser can be ascribed to its negative TO coefficient and electron-phonon coupling as suggested by several experimental and theoretical investigations<sup>[14, 41]</sup>. Elevated temperature both reduces luminous efficacy and raises the lasing threshold<sup>[46]</sup>. The maximum detectable temperature value for the NPL is around 300 K because the lasing will stop at higher temperatures.

The measurement stability of the NPL laser was also characterized. These lasing spectra (Fig. 3(c)) at  $P = 20.2\ \mu\text{J} \cdot \text{cm}^{-2}$  were measured continuously for 150 s. As can be seen, the lasing peak at 785.58 nm exhibited almost no wavelength shift. It can be seen

from the laser peak remains constant for more than 150 s, which indicates that the temperature can be precisely measured by monitoring the central wavelength of the NPL laser. Furthermore, the laser emission of the NPLs can be stable for 1 200 s<sup>[45]</sup>, the operational stability data are in agreement with most of the reported MAPbI<sub>3</sub> lasers<sup>[46-47]</sup>. Promoting the operating stability of lasers is one of the constant tasks of laser technology. Changes in microscopic images of a NPL after leaving in pure N<sub>2</sub> condition for 72 h and 144 h are shown in Fig. 4. As can be seen, the color of the NPL is still uniform after 144 h which indicates that the NPL with proper encapsulation could have better stability. Until now, great efforts have been made to improve the stability of organic-inorganic perovskites while maintaining their outstanding photophysical properties such as thermal management<sup>[18]</sup>, encapsulation<sup>[45]</sup>, passivation<sup>[48]</sup>, etc. Adopting the encapsulation and passivation strategies to improve the stability, the laser stabilization times of the NPLs would be higher than 8 500 s<sup>[45]</sup>. The compact spectrometer used has a wavelength resolution of 0.07 nm, limiting the temperature resolution of the sensor to  $0.37\ ^{\circ}\text{C}$ . In principle, by using a spectrometer with a high wavelength resolution, temperature resolution can be further improved.

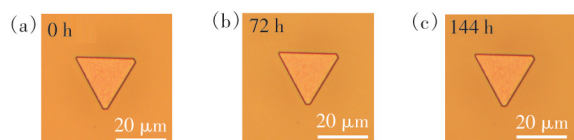


Fig. 4 Microscopic images of a NPL after leaving in pure N<sub>2</sub> condition for 0 h(a), 72 h(b) and 144 h(c), respectively

In order to meet the needs of practical applications, we have also investigated the reversibility of the perovskite NPLs-based temperature sensors during a heating and cooling cycle. Organic-inorganic hybrid perovskites generally show no phase transition upon temperature variations in the temperature range of 160–330 K<sup>[49-50]</sup>. Therefore, the NPLs can measure temperatures from 160 K to 300 K. This property makes them suitable for temperature sensors. The lasing spectra evolution during a heating and cooling cycle is shown Fig. 5 (a). The lasing

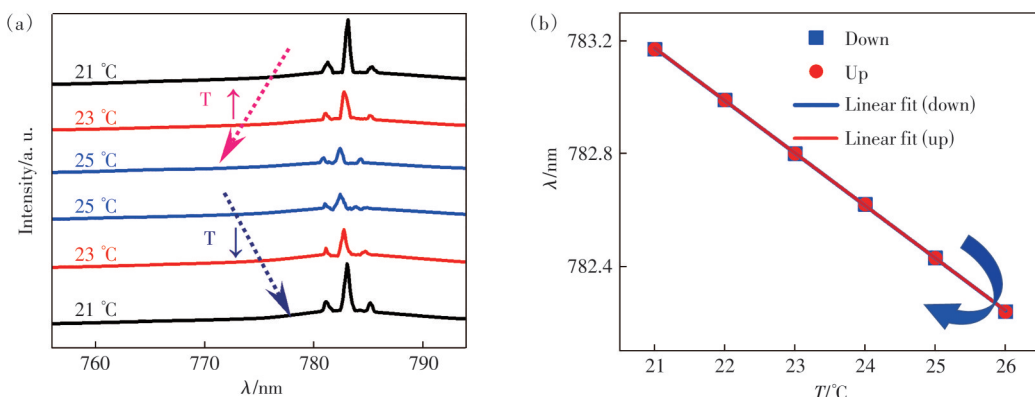


Fig. 5 (a) Recovery of laser spectral after the temperature returns to the initial point. (b) The evolution of peak wavelength of the laser with temperature in a rising and decreasing cycle

peak underwent a blueshift during the heating process, and the lasing peak can be recovered after cooling down to the original temperature. Fig. 5 (b) shows the dependence of the center wavelength of the laser on the temperature in the heating (red circles) and cooling (blue squares) cycles. It could be seen that the lasing wavelengths change linearly with temperature during the two processes, which shows that the demonstrated sensor has terrific wavelength accuracy and reversible property.

The produced triangular NPLs have different sizes and colors, as well as different edge lengths and thicknesses. Therefore, the peak wavelengths and temperature sensitivities have a slight fluctuation<sup>[44]</sup>. Fig. 6 shows the peak wavelengths and temperature sensitivity of NPLs with different edge lengths (26–38  $\mu\text{m}$ ). However, the peak wavelengths only change slightly (~ a few nm) around 781 nm. Moreover, the sensitivities also fluctuate ( $\pm 5 \text{ pm}/^\circ\text{C}$ ) only slightly around 185  $\text{pm}/^\circ\text{C}$ .

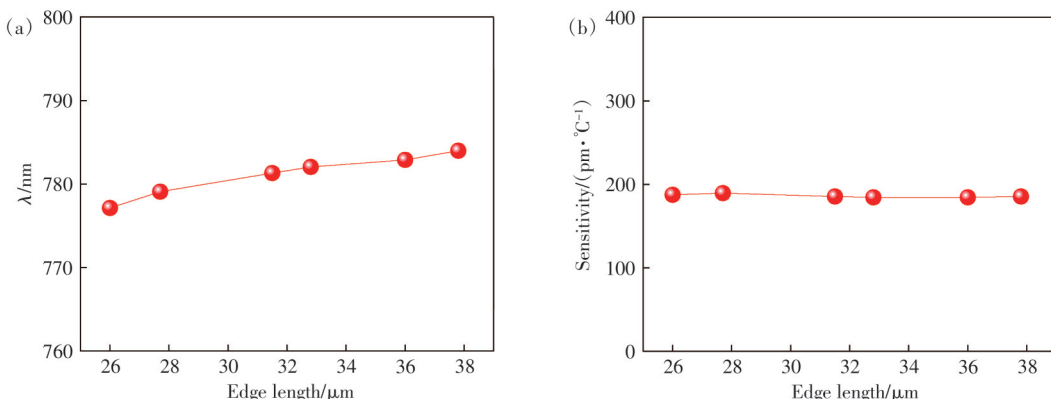


Fig. 6 (a) Peak wavelengths of NPLs with different side lengths. (b) Sensitivity of NPLs with different edge lengths

#### 4 Conclusion

This work demonstrates a submicron-scale temperature sensor based on triangular NPL lasers. The developed temperature sensor shows a high temperature sensitivity of  $\sim 185 \text{ pm}/^\circ\text{C}$  and a temperature resolution of  $\sim 0.37 \text{ }^\circ\text{C}$  (limited by the resolution of our spectrometer). It also features a low lasing threshold of  $19.8 \text{ }\mu\text{J}\cdot\text{cm}^{-2}$ , high  $Q$  up to 2 610, high stability, good reversibility, as well as a linear relation between the laser peak wave-

length and temperature. The developed submicron-scale temperature sensor is suitable for integration into flexible photothermal devices and chemical analyzers, enabling high-accuracy temperature sensing in submicron environments. Together with the high performance of the sensor, the proposed free-space optical measurement scheme, the low-cost and ease-of-fabrication properties of the active material, this work lays a solid foundation for the development and application of thermal sensing based on NPL and other metal-halide materials.

By studying and improving these materials, it will be possible to manufacture more accurate, more sensitive, and smaller temperature sensors.

Response Letter is available for this paper at:  
<http://cjl.lightpublishing.cn/thesisDetails#10.37188/CJL.20240133>.

## References:

- [ 1 ] DING H, LV G Q, CAI X, *et al*. An optoelectronic thermometer based on microscale infrared-to-visible conversion devices [J]. *Light Sci. Appl.*, 2022, 11(1): 130.
- [ 2 ] WANG Y Y, ZENG S W, HUMBERT G, *et al*. Microfluidic whispering gallery mode optical sensors for biological applications [J]. *Laser Photon. Rev.*, 2020, 14(12): 2000135.
- [ 3 ] LI G H, LIN K, ZHAO K F, *et al*. Localized bound multiexcitons in engineered quasi-2D perovskites grains at room temperature for efficient lasers [J]. *Adv. Mater.*, 2023, 35(20): 2211591.
- [ 4 ] BAI T T, GU N. Micro/nanoscale thermometry for cellular thermal sensing [J]. *Small*, 2016, 12(34): 4590-4610.
- [ 5 ] HAHM J, KIM K, QIU Y J, *et al*. Increasing ambient temperature progressively disassembles *Arabidopsis* phytochrome B from individual photobodies with distinct thermostabilities [J]. *Nat. Commun.*, 2020, 11(1): 1660.
- [ 6 ] SHIN J, LIU Z H, BAI W B, *et al*. Biodegradable optical sensor systems for monitoring of intracranial pressure and temperature [J]. *Sci. Adv.*, 2019, 5(7): aaw1899.
- [ 7 ] XU H T, HAFEZI M, FAN J, *et al*. Ultra-sensitive chip-based photonic temperature sensor using ring resonator structures [J]. *Opt. Express*, 2014, 22(3): 3098-3104.
- [ 8 ] GUAN X W, WANG X Y, FRANDSEN L H. Optical temperature sensor with enhanced sensitivity by employing hybrid waveguides in a silicon Mach-Zehnder interferometer [J]. *Opt. Express*, 2016, 24(15): 16349-16356.
- [ 9 ] WANG J, PEI L, WANG J S, *et al*. Magnetic field and temperature dual-parameter sensor based on magnetic fluid materials filled photonic crystal fiber [J]. *Opt. Express*, 2020, 28(2): 1456-1471.
- [ 10 ] LIU Y C, LI S G, CHEN H L, *et al*. Surface plasmon resonance induced high sensitivity temperature and refractive index sensor based on evanescent field enhanced photonic crystal fiber [J]. *J. Lightw. Technol.*, 2020, 38(4): 919-928.
- [ 11 ] BAI Y T, MIAO Y P, ZHANG H M, *et al*. Simultaneous measurement of temperature and relative humidity based on a microfiber sagnac loop and MoS<sub>2</sub> [J]. *J. Lightw. Technol.*, 2020, 38(4): 840-845.
- [ 12 ] YANG Y Q, WANG Y G, ZHAO Y X, *et al*. Sensitivity-enhanced temperature sensor by hybrid cascaded configuration of a Sagnac loop and a F-P cavity [J]. *Opt. Express*, 2017, 25(26): 33290-33296.
- [ 13 ] WIENHOLD T, KRAEMMER S, WONDIMU S F, *et al*. All-polymer photonic sensing platform based on whispering-gallery mode microgoblet lasers [J]. *Lab Chip*, 2015, 15(18): 3800-3806.
- [ 14 ] JIANG X F, QAVI A J, HUANG S H, *et al*. Whispering-gallery sensors [J]. *Matter*, 2020, 3(2): 371-392.
- [ 15 ] WANG P F, DING M, MURUGAN G S, *et al*. Packaged, high-Q, microsphere-resonator-based add-drop filter [J]. *Opt. Lett.*, 2014, 39(17): 5208-5211.
- [ 16 ] DE SOUSA-VIEIRA L, RÍOS S, MARTÍN I R, *et al*. Whispering gallery modes in a holmium doped glass microsphere: temperature sensor in the second biological window [J]. *Opt. Mater.*, 2018, 83: 207-211.
- [ 17 ] WAN L, CHANDRAHALIM H, CHEN C, *et al*. On-chip, high-sensitivity temperature sensors based on dye-doped solid-state polymer microring lasers [J]. *Appl. Phys. Lett.*, 2017, 111(6): 061109.
- [ 18 ] LI G H, HOU Z, WEI Y F, *et al*. Efficient heat dissipation perovskite lasers using a high-thermal-conductivity diamond substrate [J]. *Sci. China Mater.*, 2023, 66(6): 2400-2407.
- [ 19 ] LI B B, WANG Q Y, XIAO Y F, *et al*. On chip, high-sensitivity thermal sensor based on high-Q polydimethylsiloxane-coated microresonator [J]. *Appl. Phys. Lett.*, 2010, 96(25): 251109.
- [ 20 ] YOU M M, LIN Z D, LI X Y, *et al*. Chip-Scale Silicon ring resonators for cryogenic temperature sensing [J]. *J. Lightw. Technol.*, 2020, 38(20): 5768-5773.
- [ 21 ] LUO R, JIANG H W, LIANG H X, *et al*. Self-referenced temperature sensing with a lithium niobate microdisk resonator [J]. *Opt. Lett.*, 2017, 42(7): 1281-1284.
- [ 22 ] KIM E, BAASKE M D, VOLLMER F. Towards next-generation label-free biosensors: recent advances in whispering gallery mode sensors [J]. *Lab Chip*, 2017, 17(7): 1190-1205.

- [ 23 ] LEI L, DONG Q, GUNDOGDU K, et al. Metal halide perovskites for laser applications [J]. *Adv. Funct. Mater.* , 2021, 31(16): 2010144.
- [ 24 ] FRIGENTI G, BERNESCHI S, FARNESE D, et al. Rare earth-doped glass whispering gallery mode micro-lasers [J]. *Eur. Phys. J. Plus*, 2023, 138(8): 679.
- [ 25 ] TOROPOV N, VOLLMER F. Whispering-gallery microlasers for cell tagging and barcoding: the prospects for *in vivo* bio-sensing [J]. *Light Sci. Appl.* , 2021, 10(1): 77.
- [ 26 ] YANG Y, LEI F C, KASUMIE S, et al. Tunable erbium-doped microbubble laser fabricated by sol-gel coating [J]. *Opt. Express*, 2017, 25(2): 1308-1313.
- [ 27 ] ZHU S, SHI L, XIAO B W, et al. All-optical tunable microlaser based on an ultrahigh- $Q$  erbium-doped hybrid microbotle cavity [J]. *ACS Photon.* , 2018, 5(9): 3794-3800.
- [ 28 ] GUO Z H, QIN Y C, CHEN P Z, et al. Hyperboloid-drum microdisk laser biosensors for ultrasensitive detection of human IgG [J]. *Small*, 2020, 16(26): 2000239.
- [ 29 ] FABITHA K, RAMACHANDRA RAO M S. Biocompatible miniature temperature sensor based on whispering gallery modes of Sm<sup>3+</sup> activated ZnO optical micro-resonators [J]. *Appl. Phys. Lett.* , 2021, 118(16): 163104.
- [ 30 ] SHELLAIAH M, SUN K W. Review on sensing applications of perovskite nanomaterials [J]. *Chemosensors*, 2020, 8 (3): 55.
- [ 31 ] LI F M, WU D, SHANG L, et al. Highly efficient monolithic perovskite/perovskite/silicon triple-junction solar cells [J]. *Adv. Mater.* , 2024, 36(16): 2311595.
- [ 32 ] MIAO Y F, CHENG L, ZOU W, et al. Microcavity top-emission perovskite light-emitting diodes [J]. *Light Sci. Appl.* , 2020, 9: 89.
- [ 33 ] LEE Y H, SONG I, KIM S H, et al. Perovskite photodetectors: perovskite granular wire photodetectors with ultrahigh photodetectivity [J]. *Adv. Mater.* , 2020, 32(32): 2070238.
- [ 34 ] ZHU Z H, SUN Q, ZHANG Z P, et al. Metal halide perovskites: stability and sensing-ability [J]. *J. Mater. Chem. C*, 2018, 6(38): 10121-10137.
- [ 35 ] LUO P F, ZHOU S W, XIA W, et al. Chemical vapor deposition of perovskites for photovoltaic application [J]. *Adv. Mater.* , 2017, 4(8): 1600970.
- [ 36 ] WANG Y L, GUAN X, LI D H, et al. Chemical vapor deposition growth of single-crystalline cesium lead halide micro-platelets and heterostructures for optoelectronic applications [J]. *Nano Res.* , 2017, 10(4): 1223-1233.
- [ 37 ] DESCHLER F, PRICE M, PATHAK S, et al. High photoluminescence efficiency and optically pumped lasing in solution-processed mixed halide perovskite semiconductors [J]. *J. Phys. Chem. Lett.* , 2014, 5(8): 1421-1426.
- [ 38 ] HANDA T, TAHARA H, AHAREN T, et al. Large negative thermo-optic coefficients of a lead halide perovskite [J]. *Sci. Adv.* , 2019, 5(7): eaax0786.
- [ 39 ] LIAO J, YANG L. Optical whispering-gallery mode barcodes for high-precision and wide-range temperature measurements [J]. *Light Sci. Appl.* , 2021, 10(1): 32.
- [ 40 ] HAO Y H, GUO Z X. Monitor *in situ* superconducting temperature via optical whispering-gallery mode sensors [J]. *J. Phys. D Appl. Phys.* , 2019, 52(17): 175101.
- [ 41 ] FRANKLIN D, UELTSCHI T, CARLINI A, et al. Bioresorbable microdroplet lasers as injectable systems for transient thermal sensing and modulation [J]. *ACS Nano*, 2021, 15(2): 2327-2339.
- [ 42 ] ZHANG Q, HA S T, LIU X F, et al. Room-temperature near-infrared high- $Q$  perovskite whispering-gallery planar nanolasers [J]. *Nano Lett.* , 2014, 14(10): 5995-6001.
- [ 43 ] HUANG C, SUN W Z, FAN Y B, et al. Formation of lead halide perovskite based plasmonic nanolasers and nanolaser arrays by tailoring the substrate [J]. *ACS Nano*, 2018, 12(4): 3865-3874.
- [ 44 ] LI G H, CHE T, JI X Q, et al. Record-low-threshold lasers based on atomically smooth triangular nanoplatelet perovskite [J]. *Adv. Funct. Mater.* , 2019, 29(2): 1805553.
- [ 45 ] LI G H, PI H H, WEI Y F, et al. Passivation of degradation path enables high performance perovskite nanoplatelet lasers with high operational stability [J]. *Photon. Res.* , 2022, 10(6): 1440-1452.
- [ 46 ] ZHU H M, FU Y P, MENG F, et al. Lead halide perovskite nanowire lasers with low lasing thresholds and high quality factors [J]. *Nat. Mater.* , 2015, 14(6): 636-642.

- [ 47 ] WHITWORTH G L, HARWELL J R, MILLER D N, *et al.* Nanoimprinted distributed feedback lasers of solution processed hybrid perovskites [J]. *Opt. Express*, 2016, 24(21): 23677-23684.
- [ 48 ] ZHAO P J, KIM B J, JUNG H S. Passivation in perovskite solar cells: a review [J]. *Mater. Today Energy*, 2018, 7: 267-286.
- [ 49 ] WHITFIELD P S, HERRON N, GUISE W E, *et al.* Structures, phase transitions and tricritical behavior of the hybrid perovskite methyl ammonium lead iodide [J]. *Sci. Rep.*, 2016, 6: 35685.
- [ 50 ] HE Y M, ZHENG K B, HENRY P F, *et al.* Direct observation of size-dependent phase transition in methylammonium lead bromide perovskite microcrystals and nanocrystals [J]. *ACS Omega*, 2022, 7(44): 39970-39974.



赵若凡(1999-),男,山西运城人,硕士研究生,2021年于长治学院获得学士学位,主要从事微纳光电子器件方面的研究。

E-mail: noedzhaorf@163.com



李国辉(1984-),男,四川广元人,博士,副教授,硕士生导师,2011年于华东师范大学获得博士学位,主要从事包括钙钛矿激光器、表面等离激元纳米器件、有机及钙钛矿光电探测器等的研究。

E-mail: liguohui@tyut.edu.cn



陈俊生(1988-),男,四川达州人,博士,助理教授,2018年于隆德大学获得博士学位,主要从事分子自组装纳米颗粒研发用于生物成像、发光材料激发态动力学研究。

E-mail: junsheng.chen@chem.ku.dk